Variability of Cloudiness over Mountain Terrain in the Western United States

EDWIN SUMARGO AND DANIEL R. CAYAN

Scripps Institution of Oceanography, University of California, San Diego, La Jolla, California

(Manuscript received 9 August 2016, in final form 2 February 2017)

ABSTRACT

This study investigates the spatial and temporal variability of cloudiness across mountain zones in the western United States. Daily average cloud albedo is derived from a 19-yr series (1996–2014) of half-hourly Geostationary Operational Environmental Satellite (GOES) images. During springtime when incident radiation is active in driving snowmelt–runoff processes, the magnitude of daily cloud variations can exceed 50% of long-term averages. Even when aggregated over 3-month periods, cloud albedo varies by ±10% of long-term averages in many locations. Rotated empirical orthogonal functions (REOFs) of daily cloud albedo anomalies over high-elevation regions of the western conterminous United States identify distinct regional patterns, wherein the first five REOFs account for ~67% of the total variance. REOF1 is centered over Northern California and Oregon and is pronounced between November and March. REOF2 is centered over the interior northwest and is accentuated between March and July. Each of the REOF/rotated principal components (RPC) modes associates with anomalous large-scale atmospheric circulation patterns and one or more large-scale teleconnection indices (Arctic Oscillation, Niño-3.4, and Pacific–North American), which helps to explain why anomalous cloudiness patterns take on regional spatial scales and contain substantial variability over seasonal time scales.

1. Introduction

Understanding spatial and temporal variability of cloudiness is a long-standing problem (e.g., Welch et al. 1988; Seze and Rossow 1991; Rossow et al. 2002; Simpson et al. 2004). A better determination of recent historical variability is yet more important in the light of climate change, which may affect storm tracks and cloud patterns (Yin 2005; Held and Soden 2006; O'Gorman and Schneider 2008; Dettinger 2011). Cloud variability in mountain settings is enigmatic because clouds and radiation are not well monitored by surface observers, because cloudiness depends on several factors at multiple scales including storm tracks and cloud life cycles, and because topographic features can change the cloud systems on relatively short spatial and temporal scales (Rauber 1992). The present work addresses this complexity by identifying the extent to which the cloudiness in mountain zones is organized over large regional scales and how it varies temporally.

In the mountains of the western United States, precipitation is largely delivered as snow from cool season storms (Serreze et al. 1999). Snowpack provides water storage (Mote 2006) and is an integral part of the hydrologic cycle in the region (Pierce et al. 2008; Pierce and Cayan 2013). In snow-fed watersheds, net solar radiation is the primary energy input for spring snowmelt (U.S. Army Corps of Engineers 1956), providing 66%–90% of energy needed for snowmelt (Marks and Dozier 1992; Cline 1997). Varying cloudiness comes into play in modulating this solar heating and the associated snowmelt, a process that continues into the summer. In their study of hydrologic responses in the upper Colorado River basin, Mizukami et al. (2014) reported a difference of 85 $W m^{-2}$ in shortwave radiation in May, which translated to a difference of 273 mm snowmelt at elevations above 3 km, contributing to the differences of ~20% in annual runoff and ~20 days in the timing of snowmelt and runoff.

Diurnal and annual cycles of solar energy reaching the surface are controlled by solar geometry, but the anomalous solar variations depend on the structure and evolution of clouds (Kleissl 2013). Consequently, cloud cover variations are the principal regulator of solar insolation from synoptic to interannual time scales (Smith et al. 1992; Ringer and Shine 1997). Cloudiness also affects longwave radiation exchange with the surface

Corresponding author e-mail: Edwin Sumargo, esumargo@ucsd.edu

DOI: 10.1175/JHM-D-16-0194.1

(Aguado 1985). Therefore, understanding cloud variability is needed to comprehensively explain the spatial and temporal variations of surface processes, particularly the fluctuating patterns of hydrologic measures over the mountainous western United States.

Although clouds are a major regulator of the energy budget, their optical properties vary over a range of spatial scales, so describing the incoming radiation using radiative transfer modeling is not feasible (Gimeno García et al. 2012). Additionally, in situ radiation measurements are difficult in mountainous settings because complex topography and snow-laden seasons hinder necessary ground-based observations. Moreover, surface point radiation measurements generally lack the scope required to portray spatial and temporal structure over the broader region. As a result, clouds and surface radiation in mountainous terrains have been inadequately described (Gautier et al. 1980; Bales et al. 2006).

A direct impact of this inadequacy is reflected in hydrologic modeling and related applications, for example, in the Precipitation–Runoff Modeling System (PRMS; Leavesley et al. 1983; Markstrom et al. 2015), wherein daily surface air temperature range is used as a proxy for cloud cover to estimate surface radiation. This can introduce errors in water supply forecasts (Rittger et al. 2011) by producing biases in estimating snowmelt rate (Lapo et al. 2015) and runoff timing (Hinkelman et al. 2015).

Studies using spaceborne measurements have demonstrated the merit of remotely sensed snow albedo as input to a snowmelt model (Molotch et al. 2004), to investigate snow cover area under forest canopies (Raleigh et al. 2011), and to map snow cover (Rittger et al. 2013). Geostationary satellite estimates of surface irradiance are increasingly common (e.g., Cano et al. 1986; Ineichen and Perez 1999; Perez et al. 2002, 2010), since they provide the most accurate option for locations >25 km away from a ground station (Zelenka et al. 1999; Paulescu et al. 2012).

The availability of two decades of remotely sensed cloud measurements, along with an increasing reliance on remotely sensed radiation measures (e.g., Bales et al. 2006; Khan et al. 2011), motivates us to investigate the variability of cloudiness over western U.S. mountain settings. Cloud variability during the hydrologically important winter-to-summer period is emphasized here. While the occurrence of long period, globally patterned changes in cloudiness is becoming clearer (Dai et al. 2006; Warren et al. 2007; Eastman and Warren 2013; Norris et al. 2016), the 19-yr Geostationary Operational Environmental Satellite (GOES) dataset used in this study is too short to resolve such changes. Accordingly, our focus here is to understand cloudiness variability from daily to seasonal time scales.

2. Datasets

a. *GOES-West visible cloud albedo*

The cloud measures explored here are derived from NOAA GOES images collected at half-hourly intervals from 1996 to 2014. GOES captures a large swath simultaneously throughout the day (http://noaasis.noaa.gov/NOAASIS/ml/genlsatl.html). The GOES radiometer provides an albedo measure defined as the ratio of reflected to incident radiation from the surface, that is, the reflectivity. As cloud cover increases, the albedo increases and the downwelling surface radiation decreases (Ramanathan et al. 1989; Iacobellis and Cayan 2013).

This study utilizes GOES-West (*GOES-9*, *GOES-10*, *GOES-11*, and *GOES-15*) visible albedo measurements with 1-km horizontal and 30-min temporal resolutions retrieved from NOAA Comprehensive Large Array-Data Stewardship System (http://www.nsof.class.noaa.gov). The 1-km pixels are spatially aggregated to 4-km pixels to alleviate the computational burden. The GOES data in this study encompass the westernmost United States and adjacent eastern North Pacific domain (25°–50°N, 130°–113°W) and span the period 1996–2014. The albedo observations are adjusted by removing the estimated clear-sky albedo to derive cloud albedo values (section 3a).

Mountain clouds can vary considerably within the period of a day in response to synoptic events and topographically forced diurnal circulations. To minimize the impact of these shorter period variations, cloud albedo is averaged over daytime scenes [0800–1600 local standard time (LST)]. The vast majority of days (>80%) have at least 15 half-hour observations. A sampling exercise that constructed the daily average from successively smaller numbers of observations per day determined that 10 out of 17 possible half-hourly data yielded a reasonable estimate of the daytime average albedo (appendix A). The daytime average albedo is the fundamental measure of cloudiness used throughout the paper.

b. *Gridded elevation data*

Gridded elevation data with 2-min cell size are downloaded from the NOAA National Geophysical Data Center (NGDC) Geophysical Data System (GEODAS) Grid Translator Design-a-Grid website (https://maps.ngdc.noaa.gov/viewers/wcs-client/). The output latitude–longitude boxes are then interpolated to the 4-km GOES pixels using shortest distance interpolation method to discriminate the high-elevation GOES pixels from the low-elevation GOES pixels (section 3c).

c. *Reanalyzed meteorological data and low-frequency weather anomalies indices*

This study utilizes the (0.3° × 0.3°) North American Regional Reanalysis (NARR; Mesinger et al. 2006) provided by NOAA/Physical Sciences Division (PSD) to investigate the associations with larger-scale meteorological patterns. Connections between cloud variability and climate patterns are also examined using a set of low-frequency weather anomalies metrics commonly known as teleconnection indices (Wallace and Gutzler 1981; Franzke et al. 2001). These metrics include the monthly versions of Pacific–North American (PNA), the Arctic Oscillation (AO), and the Niño-3.4 indices from the NOAA Climate Prediction Center database (http://www.cpc.ncep.noaa.gov/).

3. Methods

a. *Determining the clear-sky albedo and the cloud albedo*

GOES albedo α is controlled by both clouds and other noncloud factors. The noncloud component of albedo, that is, clear-sky albedo α_{clear}, is dominated by changing surface characteristics (e.g., snow covered vs not snow covered) as well as changes in clear atmospheric components (e.g., aerosol). The cloud component of albedo, hereby called cloud albedo α_{cloud}, is determined as the difference between α and α_{clear}:

$$\alpha_{\text{cloud}} = \alpha - \alpha_{\text{clear}}. \tag{1}$$

Clear-sky albedo evolves over time in response to local albedo variations at and near the surface, chiefly consisting of snow, moisture, and vegetation (Perez et al. 2002). It is calculated and subtracted from α separately for each individual half-hour of the day since surface reflectance can be dependent on the angle of incoming solar radiation (Iacobellis and Cayan 2013). The units of the albedos are percent, ranging from 0% (transparent) to 100% (opaque).

Clear-sky albedo is derived using a sliding time window algorithm (Cano et al. 1986; Perez et al. 2002), such that α_{clear} is the minimum α observed at a particular pixel within a prescribed time window. A time window centered on a given target day [after Paech et al. (2009)] is used to determine the minimum albedo value (α_{clear}), under the likely assumption that there is at least one clear-weather day within this time window for each particular half-hour. This algorithm is based on the premise that clouds are nonstationary and thus the minimum value of daily mean α observed at each pixel can provide a reference albedo map (Cano et al. 1986), which in this case is α_{clear}. A set of time windows was investigated to determine their ability to capture fluctuations from changing surface properties. This experimentation indicated that a sliding 15-day window of ±7 days was able to balance the need to sample a long enough period to include a clear-sky day within the window and the need to make the window narrow enough to capture relatively short time-scale changes in surface characteristics (appendix B). Figure 1 illustrates the resulting α_{clear} and α_{cloud} estimates over a period that includes an abrupt deposit of snow cover during a winter storm from 30 November to 4 December 2005.

b. *Quantifying solar insolation sensitivity to cloudiness variation*

The influence of cloudiness on incoming solar radiation at the surface [hereby called shortwave flux (SWF)] is quantified from a simple sensitivity measure where SWF is a linear function of α_{cloud}:

$$\text{SWF} = (100\% - \alpha_{\text{cloud}})\text{SWF}_{\text{clear}}, \tag{2}$$

such that the response or sensitivity of SWF is determined as

$$\Delta\text{SWF} = \Delta\alpha_{\text{cloud}}(\text{SWF}_{\text{clear}}), \tag{3}$$

where $\text{SWF}_{\text{clear}}$ is theoretical clear-sky SWF calculated as a function of geolocation and time of the year (see http://maeresearch.ucsd.edu/kleissl/files/R.m for documentation). To investigate the effect of cloud variations, we evaluate the response of SWF to a 10% increase in α_{cloud} ($\Delta\alpha_{\text{cloud}} = 10\%$). The resultant linear response is presented for every season and at four representative locations spread across the western United States to examine ΔSWF at different areas and different times of the year. Additionally, the linear response derived from observed solar irradiance records from radiometers at selected Sierra Nevada sites are employed.

c. *Low-elevation mask*

Our GOES albedo dataset includes all pixels, regardless of altitude, within the western U.S.–eastern North Pacific domain. In several of our analyses, we wish to focus upon cloud variability that occurs over the higher terrain, without including stratus cloud influences and other possible valley and low-elevation effects. For these high-terrain analyses, GOES pixels with elevations of less than 800 m are masked using the gridded elevation data to focus on cloudiness over higher-elevation terrain.

d. *Removing the seasonal cycle of α_{cloud} and meteorological variables*

The estimated seasonal cycle of α_{cloud} is removed using the daily climatology (average) of α_{cloud} at each individual pixel. After considering different estimators of

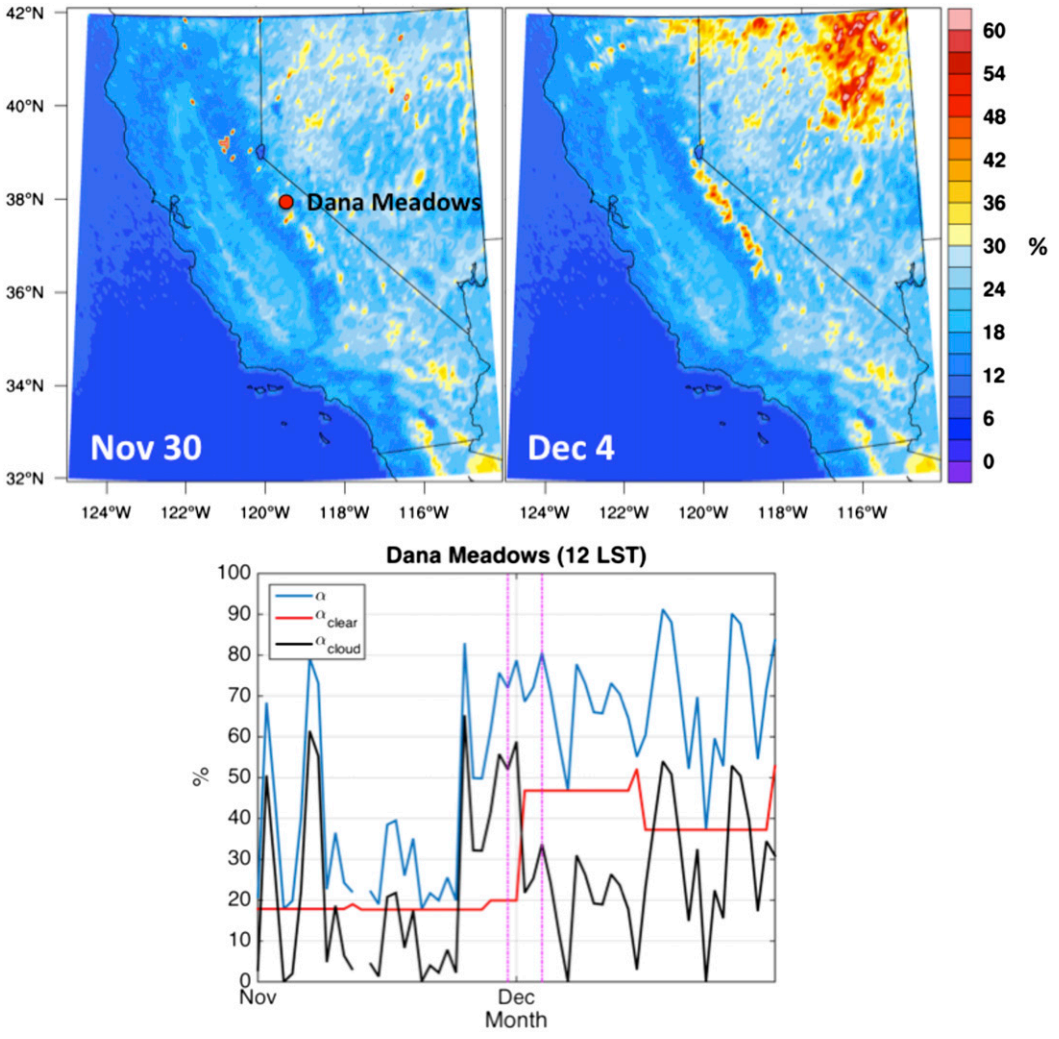

FIG. 1. (top) Estimated daily mean (0800–1600 LST) α_{clear} over California and Nevada (left) before and (right) after the 1–3 Dec 2005 snowstorm. (bottom) November and December 2005 time series of local noontime α (blue) and the estimated α_{clear} (red) and α_{cloud} (black) at GOES pixel above Dana Meadows in Yosemite National Park (37.9°N, 119.26°W; 2987 m). The vertical magenta lines denote 30 Nov and 4 Dec 2005.

the seasonal cycle, we adopt a long-term (19 years) average of the daily α_{cloud} wherein the daily average values are smoothed using a 29-day ($\pm$14 days) centered moving average to reduce high-frequency sampling noise (appendix C). The ''deseasonalized'' α_{cloud} is defined as the difference between α_{cloud} and the smoothed daily climatology. The resulting deseasonalized residuals provide a description of higher-frequency (intraseasonal) weather and climatic phenomena.

e. REOF of daily cloud anomalies

Empirical orthogonal function (EOF) analysis (Lorenz 1956; Davis 1976; Hannachi 2004) is employed to decompose space–time variations in daily α_{cloud} into orthogonal spatial eigenvector patterns (or simply EOFs) and their corresponding temporal amplitude time series, called principal components (PCs; Hannachi 2004). To ensure physically meaningful spatial structures, rotated EOFs (REOFs; Richman 1986; Hannachi 2004; Monahan et al. 2009) are constructed using Kaiser row normalization and a varimax criterion (Kaiser 1958), which are constrained to be orthogonal in time only.

The varimax rotation is applied to the five leading EOF modes of the deseasonalized α_{cloud}, all days of the year (January–December) over the 19-yr period (1996–2014), from pixels with elevations of at least 800 m above mean sea level. A set of time-varying coefficients, or rotated principal components (RPCs), was also derived. When the REOF analysis is repeated for 4-month

blocks, for example, February–May, June–September, and April–July, instead of the entire year, the results yield nearly identical patterns for the five leading REOF modes, only ordered differently according to the variance explained. In each of the 4-month and all-year analyses, the five leading modes account for 60% or more of the total variance. Moreover, the sixth mode in the all-year analysis accounts for 3.1% of the total variance, a significant drop from the fifth mode (9.5%). Therefore, only the five leading modes are presented in this paper.

f. Composites based on extreme RPC values

December–August days within the 1996–2014 period with the most positive and negative RPC values are identified to represent the cloudiest and clearest days during the winter-to-summer period when snow accumulation and melt are most active. The cloudiest days in the REOF core regions are determined as days with RPC values >90th percentile, while the clearest days are determined as days with RPC values <10th percentile. Given these subsets of cloudiest and clearest days, composites of anomaly fields of pertinent variables were formed to investigate the association of the cloudiness patterns with surface weather variables and atmospheric circulation patterns. For the latter, the NOAA/PSD website (http://www.esrl.noaa.gov/psd/cgi-bin/data/narr/plotday.pl) was used to generate NARR composite datasets corresponding to the REOF/RPC modes.

g. Contingencies based on extreme RPC values

Two-by-two contingency tables (Pearson 1904; Wilks 1995; Done et al. 2004) are constructed to examine how positive and negative anomalies of each RPC mode associate with positive and negative anomalies of the selected teleconnection indices. The days corresponding to the most positive (>75th percentile) and negative (<25th percentile) indices are identified. The cloudiest (>75th percentile) and clearest (<25th percentile) days corresponding to each RPC mode are also identified. This criterion is applied to the high positive and negative states of the AO, Niño-3.4, and PNA indices, so the cells of the two-by-two tables represent the number of days associated with high positive and negative phases of each teleconnection index and the number of days of high positive or negative phases of each RPC.

The φ coefficients and χ^2 statistics (Pearson 1904; Howell 2011) are subsequently computed to determine the correlation and statistical significance of the associations between the RPC modes and the teleconnection indices. The φ coefficient is analogous to Pearson's correlation coefficient (Pearson 1895), although it must be noted that the maximum value of φ is not necessarily ± 1 (Davenport and El-Sanhurry 1991).

4. Results and discussion

a. Variability of α_{cloud} on daily to interannual time scales

The magnitude of α_{cloud} variations at daily and interannual time scales is investigated by computing the mean μ, standard deviation σ, and the coefficient of variation (CV = σ/μ) of α_{cloud} for winter (DJF), spring (MAM), summer (JJA), and autumn (SON), separately, at each GOES pixel (all elevations) across the western United States from the 1996–2014 data. The maps showing the 3-month aggregates of σ and CV are displayed in Fig. 2 for intraseasonal daily anomalies and in Fig. 3 for interannual seasonal anomalies. The mean values are identical in both intraseasonal and interannual cases, so they are displayed in Fig. 2 only. Figures 2 and 3 illustrate DJF, MAM, and JJA to focus on periods when cloudiness variability has the most important influence on snowpack dynamics. The figures include offshore regions to compare coastal and lowland cloud variability to that of the higher-elevation terrestrial regions of the western United States. The albedo mean and variability statistics of representative regions for all four seasons are presented in Table 1.

Seasonal means of α_{cloud} range from as low as 6% to as high as 30%. Cloudiness is greatest in the offshore and nearshore coastal lowlands, and over mountainous terrains of the Pacific Coast Range, the Cascades, the northern Rockies, and the Sierra Nevada (Fig. 2, top). Over land, cloudiness tends to be greater north of San Francisco than to its south. A well-defined seasonality is observed over much of the western U.S. landmass, with greatest cloudiness in winter and least in summer. This contrasts with offshore and coastal lowland marine cloudiness in California, which peaks in summer (Clemesha et al. 2016) and illustrates the distinct physical mechanisms driving cloud formations. While subsiding air masses and low-level inversions are involved in marine layer clouds, synoptic-scale weather systems, for example, Pacific cold fronts, are the primary generator of cool season mountain clouds. These synoptic systems produce spatially coherent cloudiness from offshore Pacific Northwest to the Cascades and Sierra Nevada.

The variability of daily α_{cloud}, represented by σ (Fig. 2, middle), ranges from ~2% to >20%. On daily time scales, σ is highest over the coastal ocean and coastal lowlands and over the western slopes of

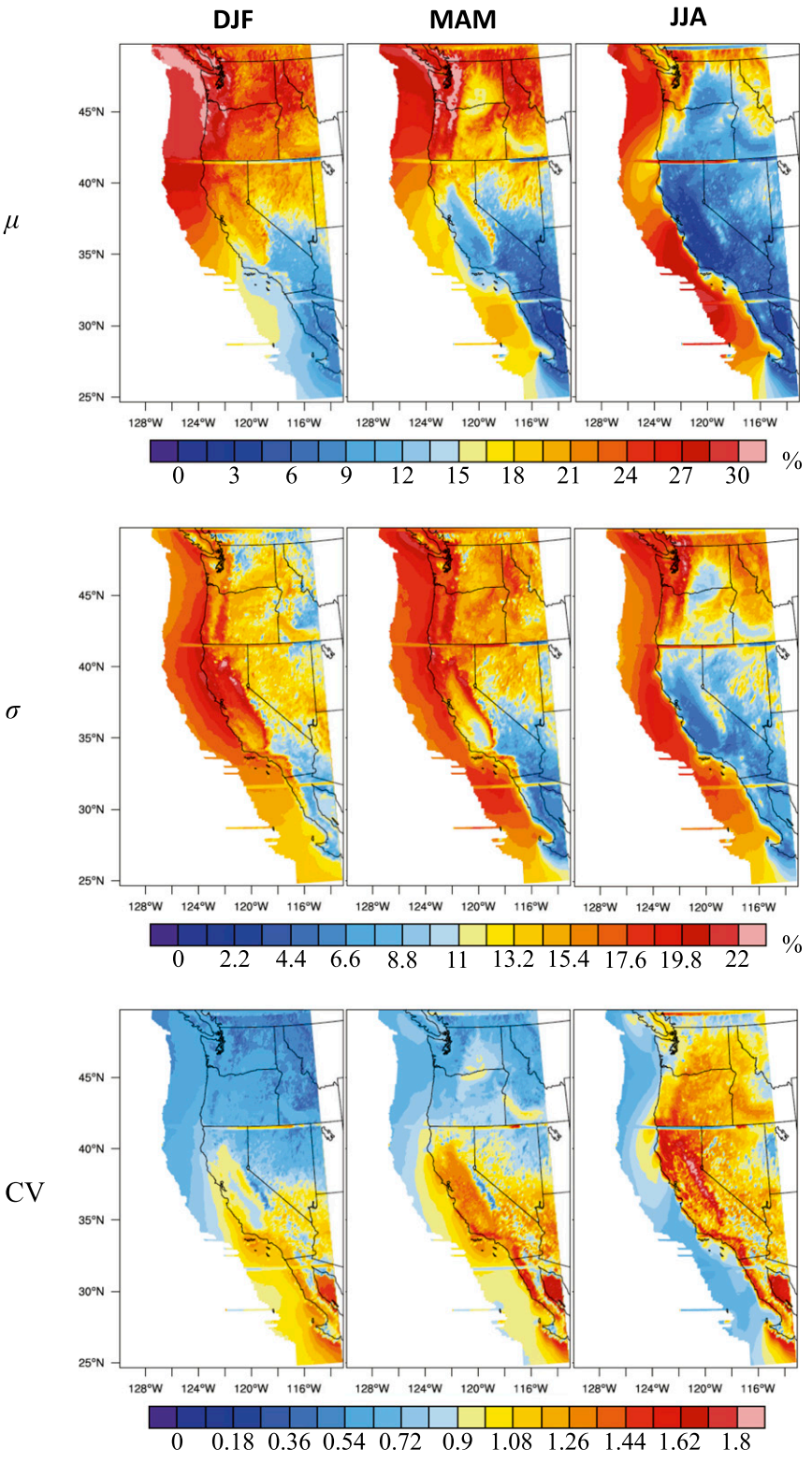

FIG. 2. Maps of (top) mean, (middle) std dev, and (bottom) CV of daily α_{cloud} for (left) winter (DJF), (center) spring (MAM), and (right) summer (JJA).

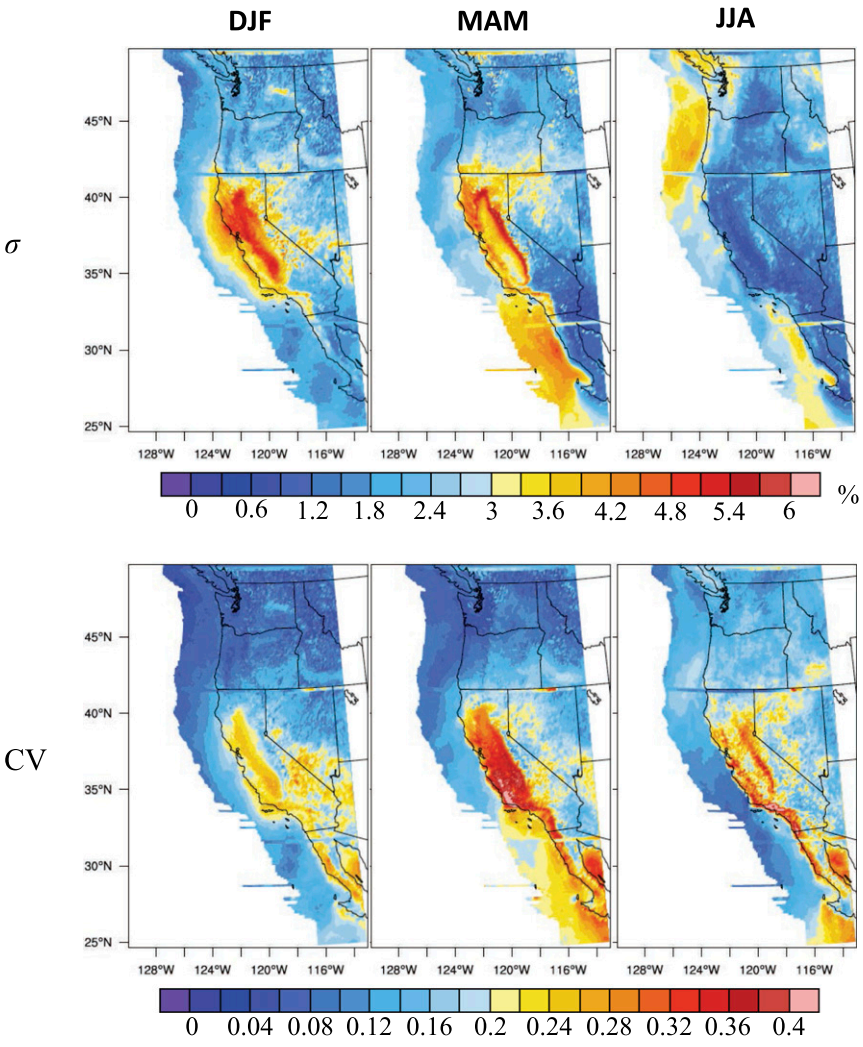

FIG. 3. (top) Std dev and (bottom) CV for (left) winter (DJF), (center) spring (MAM), and (right) summer (JJA) calculated from seasonal (3 month) α_{cloud} averages. Means for the seasonal averages are same as those in Fig. 2, so are not shown. Note change in color scales from those in Fig. 2.

mountain ranges. Regions with greater μ usually exhibit greater daily σ, including inland areas in California where both daily μ and σ are high in winter and spring. In California, this pattern demonstrates the strong influence of synoptic weather patterns in determining the enhanced average and time-varying cloudiness in winter and spring months. However, over the interior Pacific Northwest in winter and spring, μ is high but σ is reduced, suggesting more persistent cloudiness. In the interior Pacific Northwest, the variability is heightened in summer and rather isolated from that over the coasts, indicative of regional processes including local convective activities.

Daily α_{cloud} CVs (Fig. 2, bottom) provide a different perspective of the variability since they are scaled by their mean values, so a higher CV denotes increased variability relative to average conditions. The CV is generally higher in the south than in the north, an indication of the important role played by time-varying cloudiness in a region with lower overall mean cloudiness such as the southwestern United States, or particularly California. In DJF and MAM, the daily CV is pronounced along the eastern side of the Sierra Nevada rather than along the Sierra Nevada range itself, probably related to the irregular occurrence of mountain cloud formations, including the wave cloud that Grubišić and Billings (2008) found in spring and, even more variably, in winter. The high CV in California continues through JJA, which reflects the intermittent orographic thunderstorms that are common over the plateaus and mountains of the western

TABLE 1. Daily and seasonal mean and std dev of α_{cloud} (%) and the CV for winter (DJF), spring (MAM), summer (JJA), and autumn (SON). The two tabulations are aggregates over the mountains in California and Oregon and over the mountains in Idaho, Montana, and eastern Washington.

		Region 1 (California–Oregon)			Region 2 (Idaho–Montana–Washington)		
Time scale	Season	μ	σ	CV	μ	σ	CV
Daily	DJF	22.4	11.3	0.50	24.7	8.1	0.33
	MAM	19.8	13.0	0.66	24.8	12.1	0.49
	JJA	9.1	8.6	0.94	16.5	12.2	0.74
	SON	14.9	11.5	0.77	22.3	13.8	0.62
Seasonal	DJF	22.4	2.6	0.12	24.7	1.2	0.05
	MAM	19.8	2.8	0.14	24.8	1.4	0.06
	JJA	9.2	1.2	0.13	16.6	2.1	0.12
	SON	14.8	2.3	0.15	22.1	1.9	0.09

United States during summertime (Kelly et al. 1985; Whiteman 2000).

Turning to seasonal time scales (Fig. 3), it is important to know how much variability remains when α_{cloud} is time averaged, since persistent fluctuations of incoming radiation could affect seasonal anomalies of precipitation, snowmelt, and other surface processes. Although their magnitudes are reduced, σ and CV patterns derived from ~90-day average α_{cloud} are qualitatively similar to those from daily α_{cloud}, but they are accentuated in different regions. Importantly, the seasonal σ tends to be greatest in California, in contrast to daily σ, which is generally greatest in the Pacific Northwest. This daily–seasonal contrast indicates the regional significance of seasonal α_{cloud} variability in California, especially during snowmelt season when the variability is emphasized over the west of Sierra Nevada.

From year to year, seasonal α_{cloud} deviations range from about 4% to 40% of mean α_{cloud}, as shown by the seasonal CV (Fig. 3, bottom). Traversing central California, seasonal CVs exceed 0.18 from the California coast across the Central Valley and up the Sierra Nevada slope, and also over neighboring high elevations of western Nevada, southern Oregon, and southern Idaho. In contrast, over the Pacific Northwest, seasonal CVs are low in DJF and MAM, reflecting high mean cloudiness and relatively low interannual variation.

b. *Sensitivity of solar insolation to cloudiness variability*

Using Eq. (3), the change in SWF associated with a given change in α_{cloud} can be determined. Considering a set of selected locations (Table 2), the magnitude of daytime (0800–1600 LST) average ΔSWF, expressed as the response of SWF to a 10% increase in α_{cloud}, ranges from ~66 to ~84 W m^{-2} over spring and summer when snowmelt activity is prominent; this range of ΔSWF is representative of ΔSWF determined for a larger set of 239 high-altitude (≥800 m) locations (64–84 W m^{-2}). Furthermore, these calculated responses are comparable to those directly observed at the surface, via a least squares regression analysis, between α_{cloud} and surface pyranometer SWF at high-elevation stations in California. For example, a 10% increase in α_{cloud} at Dana Meadows and at nearby Tuolumne Meadows (37.873°N, 119.35°W; 2621 m) results in a 77–91 W m^{-2} SWF reduction over spring and summer.

c. *Coherent patterns of daily α_{cloud} variability*

To extract the dominant patterns of cloud variability over the mountains of the western United States, REOF

TABLE 2. Change in daily solar irradiance (i.e., SWF) at the surface corresponding to a 10% increase in daily α_{cloud} estimated for two locations in Region 1 [Dana Meadows, CA (37.9°N, 119.26°W; 2987 m), and Fish Lake, OR (42.38°N, 122.35°W; 1420 m)] and two locations in Region 2 [Crater Meadows, ID (46.56°N, 115.29°W; 1817 m), and Quartz Peak, WA (47.88°N, 117.09°W; 1433 m)]. A negative ΔSWF denotes reduced SWF associated with increased α_{cloud}. The sensitivity values are based on daily time series of α_{cloud} and SWF_{clear}. The daily SWF_{clear} is an average of hourly SWF_{clear} during daytime only (0800–1600 LST).

		ΔSWF (W m^{-2})			
Season	$\Delta\alpha_{cloud}$ (%)	Dana Meadows	Fish Lake	Crater Meadows	Quartz Peak
DJF	10	−43.3	−35.3	−29.8	−27.6
MAM	10	−76.4	−70.2	−67.5	−65.8
JJA	10	−84.1	−78.9	−77.5	−76.1
SON	10	−56.2	−49.0	−43.9	−42.1

TABLE 3. The eigenvalues of α_{cloud} REOF/RPCs 1–5 and the specific geographical areas where each mode is pronounced. The eigenvalue represents the amount of variance explained by each mode.

REOF/RPC	Eigenvalue (%)	Geographical emphasis
1	20.4	Northern California and Oregon
2	15.1	Interior Pacific Northwest
3	11.2	Coastal Pacific Northwest
4	10.5	Southwestern United States
5	9.5	Great Basin

analysis is performed on the deseasonalized daily α_{cloud} over high-elevation (≥800 m) terrain, encompassing all months (January–December) of 1996–2014. By design, the leading REOF patterns are the ones whose α_{cloud} anomaly patterns occupy a relatively large spatial scale and thus avoid the complexity introduced by smaller-scale, higher-order patterns. Collectively, these five REOFs account for a considerable amount of the variability of mountain cloudiness, amounting to 66.7% of the total daily variance (Table 3).

Correlations between the five leading RPCs and deseasonalized α_{cloud} are strongest over high-elevation areas where the REOFs are accentuated and rapidly degrade over adjacent lower-elevation areas (Fig. 4). REOF1 represents daily α_{cloud} anomalies that are pronounced in the mountainous region of Northern California and Oregon, including the Sierra Nevada and the Oregon Cascades. REOF2 represents daily α_{cloud} anomalies centered over the interior northwest covering Idaho, western Montana, eastern Oregon, and eastern Washington. REOF3 is concentrated over the Cascade mountain range in western Oregon and Washington. REOF4 has greatest weightings in Southern California, Nevada, and parts of Utah and Arizona. REOF5 represents daily α_{cloud} anomalies focused on the eastern two thirds of Nevada and Idaho. Each of the five leading REOFs has core areas that partially overlap with those of other REOFs because, unlike in EOF analysis, the spatial orthogonality has been relaxed in REOF analysis. For instance, both REOF1 and REOF2 contain a footprint over northeastern Oregon.

When a separate REOF analysis was applied to daily α_{cloud} anomalies over all elevations (not shown), the same five higher-elevation-oriented modes appeared, but not in the same order and in the midst of other REOFs that represent lower-elevation cloudiness, primarily over the eastern Pacific Ocean and coastal lowlands. This confirms the authenticity of the original α_{cloud} REOFs and the distinction between these higher-elevation modes from those that are organized over lower elevations.

While there is some degree of spatial overlap between the five REOFs, by construction their temporal variability is statistically independent—the RPCs are temporally orthogonal. Although each RPC has a time mean of zero for each day of the year, the magnitude of month-to-month RPC fluctuations still contains substantial seasonal variability, as shown by their monthly standard deviations (Fig. 5).

The variability of RPC1, RPC3, and RPC4 exhibits a well-defined annual cycle, while that of RPC2 and RPC5 displays a biannual cycle peaking in spring and early autumn. The Oregon–California and Nevada modes (RPC1 and RPC4) have greatest variability between autumn and late spring and the least variability in summer. This seasonality reflects the winter-dominated storminess climate pattern in California and Nevada,

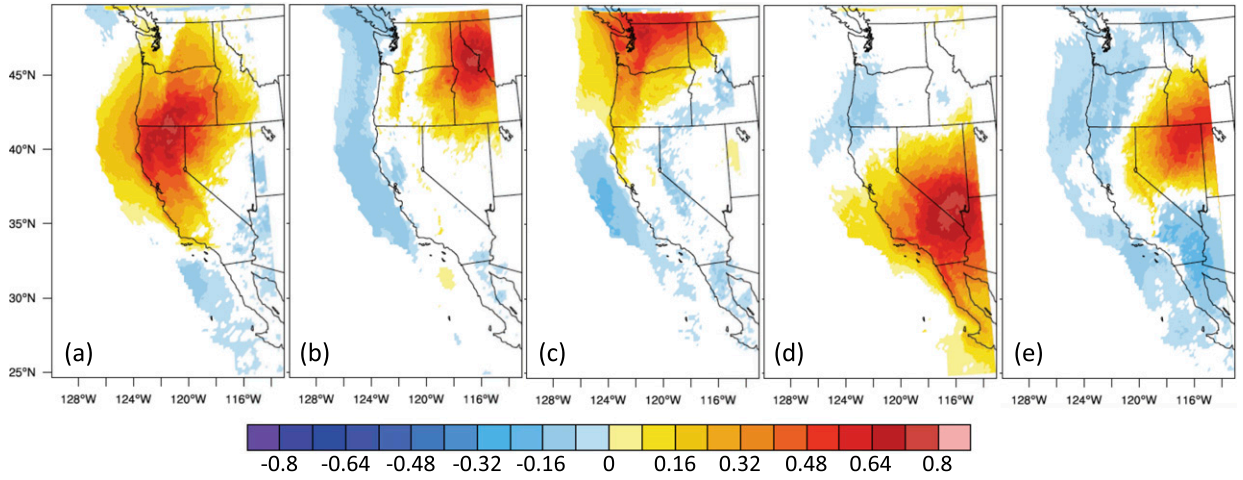

FIG. 4. Correlation fields (all months of 1996–2014) between deseasonalized daily α_{cloud} and (a) RPC1, (b) RPC2, (c) RPC3, (d) RPC4, and (e) RPC5 over the entire domain. Only pixels with p value <0.05 are colored.

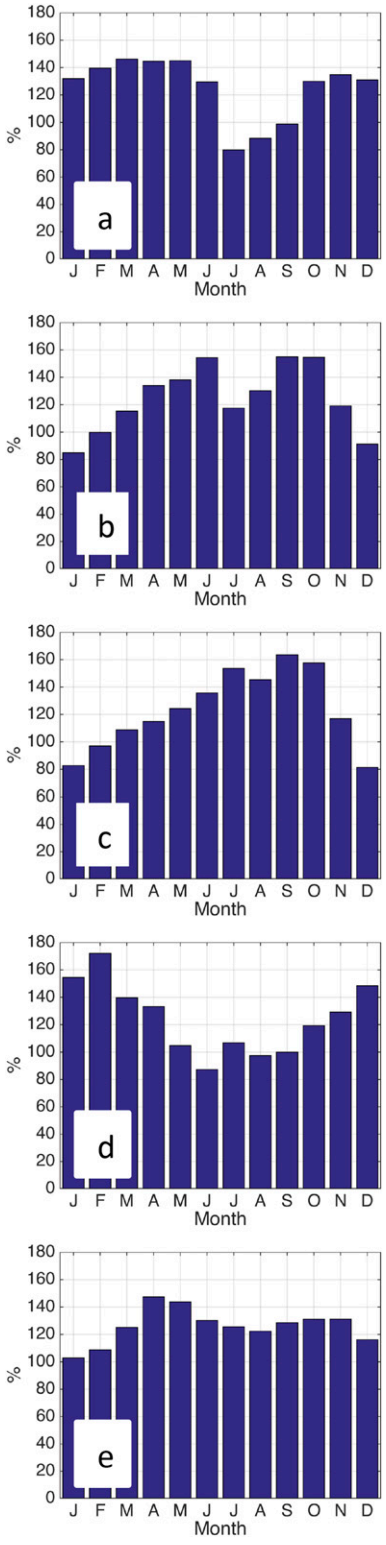

FIG. 5. Std dev of (a) RPC1, (b) RPC2, (c) RPC3, (d) RPC4, and (e) RPC5 for each month in α_{cloud} percent units, exemplifying the seasonal structures of each RPC mode.

having more abundant clouds (and higher variations thereof) during the cool season (October–May) than during the warm season (June–September). In contrast, the two Pacific Northwest modes (RPC2 and RPC3) contain highest variability from summer to early autumn and lowest variability in winter and spring. The cloud cover over the Pacific Northwest during the cool season is high (Fig. 2, top), but prone to persisting for long periods—both RPC2 and RPC3 have minimum variability in December and January. The seasonality of the variance of the Great Basin mode (RPC5) has peaks in spring and autumn, resembling that of the northern Idaho–eastern Washington–eastern Oregon mode (RPC2) in which a twice-yearly cycle is presented.

d. *Relations to larger-scale circulation patterns*

The contours in Figs. 6a and 6b present the 500-hPa geopotential height Z_{500} composite anomaly fields from historical NARR associated with the two REOF/RPC modes during the most positive α_{cloud} RPC amplitudes (cloudiest days) during December–August. The cloudy-day composites are characterized by negative Z_{500} anomalies with centers positioned west and/or north of the strongest REOF loadings, conducive to anomalous cyclonic flow and rising motion, as described below. Similarly, the contours in Figs. 6c and 6d show the Z_{500} anomaly fields during the most negative RPC amplitude (clearest days). The clear-day composites are nearly the mirror image patterns of their positive RPC cloudy-day counterparts, with positive Z_{500} anomalies in the upstream or overlying regions, conducive to anomalous anticyclonic motion and descending motion.

The color shades in Fig. 6 represent the 500-hPa pressure vertical velocity $\boldsymbol{\omega}_{500}$ composite anomalies in association with the positive and negative α_{cloud} RPC subsets. A negative $\boldsymbol{\omega}_{500}$ anomaly denotes greater than average upward motion, often associated with lowered surface pressure and often with precipitation; a positive $\boldsymbol{\omega}_{500}$ anomaly denotes more downward motion, often associated with surface high pressure and often with fewer clouds. A consistent feature of the composites is the association of core positive REOF (greatest cloudiness) areas with strong negative $\boldsymbol{\omega}_{500}$ anomaly over areas with strong negative Z_{500} anomaly and vice versa, in agreement with canonical quasigeostrophic theory (e.g., Holton 2012).

e. *Relations to lower-frequency climate variability patterns*

The associations of the REOF/RPCs with seasonal atmospheric circulation patterns are explored using conventional teleconnection indices and correlation patterns averaged over winter (DJF), spring (MAM), and summer (JJA).

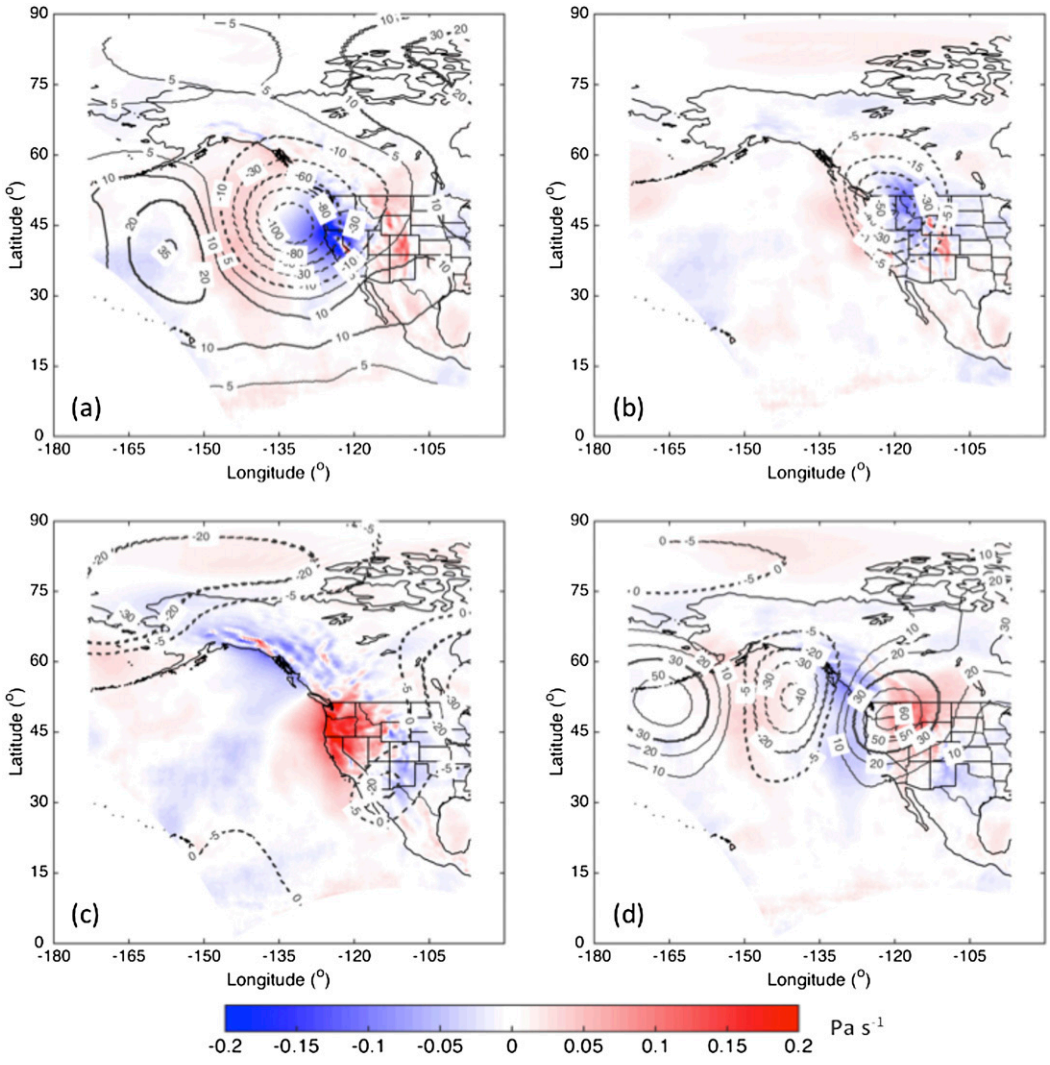

FIG. 6. The 500-hPa geopotential height anomaly (isolines) and pressure vertical velocity anomaly (shades) composited for days with the (a),(b) most positive and (c),(d) most negative anomalies for (left) RPC1 and (right) RPC2, representing cloudiest and clearest days during December–August 1996–2014. The positive (negative) Z_{500} anomaly is contoured as solid (dashed) line.

Contingency tables are developed to understand how the high and low seasonal anomalies of the α_{cloud} RPCs associate with positive and negative expressions of the teleconnection patterns. Positive (negative) cloudiness RPC anomalies represent greater (lesser) cloudiness in the respective REOF core regions and are denoted +RPCs (−RPCs). Likewise, the positive/negative phase of the teleconnection indices are marked with a plus or minus sign. From the contingency tables (not shown), the χ^2 statistics and the associated φ coefficients are summarized in Tables 4 and 5 to denote the statistical significance and the correlation of the associations between the teleconnection indices and the RPC modes.

RPC1, the interior California and Oregon pattern, has statistically significant relationships ($\chi^2 > 3.84$) with AO and PNA. RPC1 is negatively correlated with AO in DJF and JJA as indicated by the φ coefficient. Thus, +RPC1 cases tend to coincide with −AO, the equatorward and more distorted version of the high-latitude westerlies that presumably increases storminess across the midlatitudes of western North America (Thompson and Wallace 2000, 2001). The opposite pattern, −RPC1 cases, is associated with +AO, the mode having confined high-latitude westerly winds. The significant RPC1 relationship with PNA in JJA is rather unexpected because the PNA pattern is usually weak in summer, and because a high pressure ridge (indicative of fair weather) along the western North America often characterizes +PNA condition (Wallace and Gutzler 1981). The RPC1–PNA

TABLE 4. The χ^2 values of the contingency tables relating the five RPC modes to selected teleconnection indices during winter (DJF), spring (MAM), and summer (JJA) of 1996–2014. The statistic is significant at 95% confidence level when $\chi^2 > 3.84$ (boldface numbers).

Indices	Season	RPC1	RPC2	RPC3	RPC4	RPC5
AO	DJF	**23.65**	**6.72**	**6.40**	**19.46**	0.61
	MAM	0.49	1.98	0.03	0.67	0.22
	JJA	**5.13**	**4.52**	0.50	1.21	2.31
Niño-3.4	DJF	0.69	1.15	0.48	**19.51**	**5.72**
	MAM	0.00	0.79	0.15	**5.07**	0.03
	JJA	0.79	**4.38**	**5.76**	1.63	0.35
PNA	DJF	0.19	0.31	3.08	1.70	**4.13**
	MAM	1.51	0.41	0.05	2.87	0.29
	JJA	**17.49**	3.24	0.44	2.14	**17.01**

contingency table shows a particularly high number of days when both RPC1 and PNA index are negative (Table 6). This unexpected RPC1–PNA relationship in JJA may also be a "false positive" attributed to the 95% confidence level test applied here.

RPC2, the interior northwestern U.S. pattern, associates with AO in DJF and JJA, where +RPC2 tends to concur with +AO in DJF and with −AO in JJA as indicated by the φ coefficient. Although midlatitude storm activities in the North Pacific are often associated with −AO when the westerlies are usually weaker (Thompson and Wallace 2001), the relatively northern REOF2 region is in a location where the storm track may trail into the region even with +AO. Interestingly, RPC2 is positively correlated with Niño-3.4 in JJA, although El Niño–Southern Oscillation (ENSO) signal in the western United States tends to be weak in boreal summer. The RPC2–Niño-3.4 contingency table shows a particularly high number of days when both RPC2 and Niño-3.4 index are positive (Table 7), demonstrating that contingency table analysis can report a statistically significant relationship even with only one distinctly high number of days.

TABLE 5. The φ coefficients associated with the χ^2 statistics, indicating the magnitude and the sign of the correlations between the RPCs and teleconnection indices during winter (DJF), spring (MAM), and summer (JJA) of 1996–2014.

Indices	Season	RPC1	RPC2	RPC3	RPC4	RPC5
AO	DJF	−0.24	0.12	0.12	−0.22	0.04
	MAM	−0.03	0.07	−0.01	−0.04	0.02
	JJA	−0.10	−0.10	−0.03	0.05	−0.07
Niño-3.4	DJF	0.04	−0.05	−0.03	0.21	−0.11
	MAM	0.00	0.04	−0.02	0.10	−0.01
	JJA	0.04	0.10	−0.11	0.06	0.03
PNA	DJF	−0.02	−0.03	0.08	0.06	−0.10
	MAM	0.06	−0.03	−0.01	0.08	0.02
	JJA	0.20	0.09	−0.03	0.07	0.19

TABLE 6. Contingency table showing the relationship between RPC1 and PNA in JJA.

	+RPC1	−RPC1	Total
+PNA	123	78	201
−PNA	103	146	249
Total	226	224	450

Similar to RPC2, RPC3, the Cascade Range pattern, is positively correlated with AO in DJF, in keeping with the positive AO correlations with RPC2. However, the RPC3 relationship with AO is not statistically significant in JJA. The +RPC3 is negatively correlated with Niño-3.4 in JJA. In view of the fact that its neighboring interior northwest pattern (REOF2/RPC2) is positively correlated with Niño-3.4 in JJA, this indicates a rather strong gradient of cloudiness may set in during summer ENSO events.

RPC4, the southwestern U.S. pattern, is significantly correlated with AO in DJF, where, similar to +RPC1, +RPC4 tends to coincide with −AO. Furthermore, +RPC4 events are associated with +Niño-3.4 in DJF and MAM, a signature of El Niño conditions and increased storminess in the southwestern United States (Cayan et al. 1999).

RPC5, the northern Nevada and Idaho pattern, associates with Niño-3.4 and PNA. RPC5 is negatively correlated with Niño-3.4 in DJF, evidently because El Niño forces storm tracks farther south, resulting in variable influences on Great Basin precipitation (Smith et al. 2015). RPC5 is negatively correlated with PNA in DJF, indicating that strengthened high pressure ridging in winter reduces cloud cover over the northern Great Basin. However, RPC5 is positively correlated with PNA in JJA, reflecting the finding of Leathers et al. (1991) that PNA is negatively correlated with precipitation over much of the western United States during the cool season and positively correlated during the warm season.

The correlation maps between the seasonal averages of the five leading α_{cloud} RPCs and those of Z_{500} anomaly are shown in Fig. 7. Although they vary somewhat with season, the spatial structure of the correlation maps of RPC1 and RPC2 (Fig. 7) is in good

TABLE 7. Contingency table showing the relationship between RPC2 and Niño-3.4 in JJA.

	+RPC2	−RPC2	Total
+Niño-3.4	138	98	236
−Niño-3.4	102	108	210
Total	240	206	446

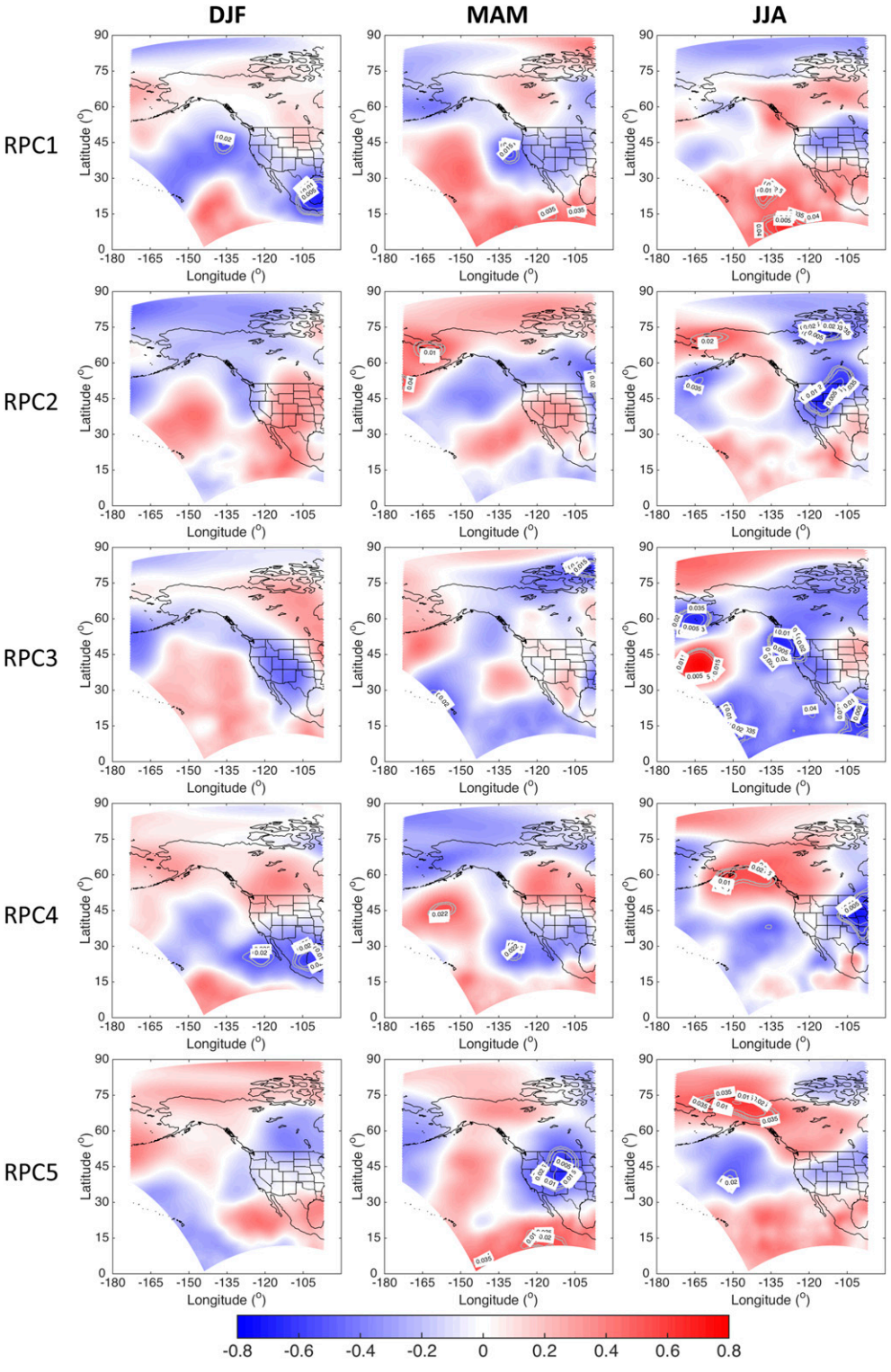

FIG. 7. Correlation maps between the seasonal averages of the five leading α_{cloud} RPCs and those of Z_{500} anomaly for 1996–2014. The gray contours denote the areas where p value <0.05.

agreement with the daily composite maps in Fig. 6. The rather detailed regional structure of the correlation maps explains why the association of western U.S. cloudiness with the AO, Niño-3.4, and PNA teleconnection patterns is perhaps more modest than might be expected. These correlations clearly represent regional circulations that may, at times, conflict with the larger-scale circulations of the major teleconnection patterns, making for relatively weak associations.

5. Summary and conclusions

Aside from having substantial spatial and seasonal variation, cloudiness over the mountains of the western U.S. has significant anomalous variation over a broad range of scales. A 19-yr (1996–2014) GOES cloud albedo (i.e., α_{cloud}) dataset, sampled to cover elevations $\geq$800 m, exhibits anomalous fluctuations whose dominant patterns are organized over regions of hundreds of kilometers. The high degree of spatial coherence is evident by the α_{cloud} REOF decomposition of the daily cloudiness variability in which the first five modes account for ~67% of the total variance. These α_{cloud} modes operate throughout the whole year, but they are modulated seasonally. For example, the leading mode represents the variability over Northern California and Oregon and is accentuated between November and March, while the second mode represents the variability over the interior Pacific Northwest and is pronounced between March and July.

Anomalous cloudiness over high-elevation regions has differing levels and primary seasons of activity. For example, in the southwest, mountain cloudiness variability is highest in spring, probably because of year-to-year climate variability and intermittent synoptic weather systems from the Pacific. This springtime variability amounts to ~13% (cloud albedo unit) on a daily scale, equivalent to ~95 W m^{-2} difference in solar radiation (based on Tables 1 and 2). Even when seasonally averaged, the α_{cloud} standard deviation amounts to ~3%, equivalent to ~20 W m^{-2} departure in incoming solar radiation. In contrast, in the northwest, the variability is lowest in winter and highest in summer, probably because it is persistently cloudy in winter while summertime cloudiness is more often interrupted by interludes of clear skies. In a relative sense, the amount of cloudiness variation compared to the mean cloudiness is uniformly higher in the southwest than in the northwest. Importantly, this relative variation is quite large, with a magnitude of up to ~1.8 on a daily scale and ~0.4 on a seasonal scale, and is typically greatest during spring and summer when snowmelt is most active.

The seasonal variability of cloudiness over mountain regions in the western United States contrasts with that of the eastern North Pacific and low-lying coastal cloudiness, reflecting the different dynamics operating in these environments. This contrast is most evident in California, where the mean cloudiness and variability over higher-elevation terrain is greatest in winter, while offshore and along the coastline they are greatest in summer.

As expected, daily variations in cloudiness are dictated by anomalous patterns of atmospheric circulation. Positive regional cloudiness anomalies are usually accompanied by anomalously low surface pressure systems, for example, negative geopotential height anomalies and upward vertical velocity anomalies.

These circulation patterns are affected by regional and, to some extent, Pacific basin-scale climate variability as represented by regional atmospheric circulation composites and by associations with AO, PNA, and Niño-3.4 teleconnection patterns. These associations vary with regions and seasons. For instance, during the winter and spring the southwestern United States is greatly influenced by AO and Niño-3.4, while the interior Pacific Northwest is almost singularly influenced by AO. Somewhat surprisingly, Northern California and Oregon are not strongly influenced by ENSO, probably because this region resides near the hinge point of the West Coast precipitation dipole (Dettinger et al. 1998).

Previous studies (e.g., Eastman and Warren 2013; Norris et al. 2016) suggest there may be a slight decline in cloud cover globally and a poleward movement of midlatitude storm tracks, but the 19-yr GOES dataset is too short to form realistic estimates of trends. Determination of long-term changes over high elevations of the western United States must contend with considerable shorter-period variability of cloudiness that is described here. Because of strong influences by large-scale weather and short-period climate patterns, cloudiness varies over regional spatial scales, with characteristic patterns that cover large portions of the high-elevation zones of the region.

Acknowledgments. E.S. was funded by the California Department of Water Resources Award 4600010378. Parts of D.R.C.'s contributions were funded by the California Energy Commission Contract CEC-500-14-005; by the U.S. Geological Survey via the Southwest Climate Science Center, Grant G13AC00336; and by NOAA via the CNAP RISA project, Grant NA11OAR4310150. Many thanks to Sam Iacobellis for providing access to GOES imagery and for useful

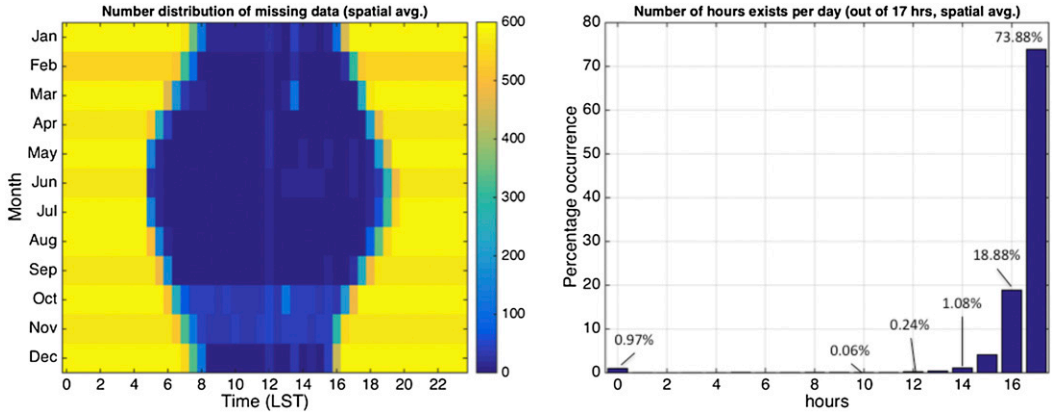

FIG. A1. (left) Number distribution of missing data for each month and half-hour of the day of 1996–2014, averaged over >300 high-elevation pixels across the westernmost United States, illustrating which hours of the day have the least/most missing data in each month. (right) The percentages of hours between 0800 and 1600 LST exist per day during the same period and averaged over the same pixels, illustrating how many daytime hours exist on average.

discussions and to Joel R. Norris and three anonymous reviewers for the thoughtful comments.

APPENDIX A

GOES Data Availability

The structure of the missing data is illustrated in Figure A1. Most of the missing data occur in early morning and late afternoon during times of low sun angle. There are more missing data in winter months because of shorter day lengths. Figure A1 (right) shows that >80% of the days have >15 half-hour daytime observations.

Whether 10 out of 17 half-hours made a reasonable daily mean estimate was determined from an analysis summarized in Table A1. We identified the days when there were no missing data between 0800 and 1600 LST and derived the daily averages. We then randomly removed (1, 2, 3…16) half-hours of the same days and rederived the daily averages. In each instance, the correlation R, root-mean-square error (RMSE), and fractional mean absolute bias ($f|\text{Bias}| = |\alpha_{17-n} - \alpha_{17}|/\alpha_{17}$, for $1 \le n \le 16$) between the two sets (with missing data vs without missing data) were computed to determine the validity of the daily averages.

There is no set standard of how many half-hours or of how much error/bias can be tolerated. Together with the facts that >90% of the days had >15 half-hours available and that the days with 7 missing data accounted for <0.1%, having an error (fractional bias) of ~1.91% (0.1) was a reasonable limit.

APPENDIX B

Clear-Sky Albedo Time Window

Figure B1 shows how different time windows used to determine the clear-sky albedo evolve throughout the water year 2006, in comparison to snow water equivalent (SWE) at nearby snow sensors in California and Idaho mountain settings. Each of the clear-sky albedos generally captures the snow and nonsnow season, but the one with the shortest time window (7 days) is hypersensitive to short-term fluctuations. In contrast, the one with the longest time window (28 days) is hyposensitive to such fluctuations. The 15-day (±7 days) time window has intermediate properties that capture

TABLE A1. The correlation, RMSE, and fractional mean absolute bias ($f|\text{Bias}|$) between daily average cloud albedo when no half-hour between 0800 and 1600 LST is missing and that when one or more (n) half-hours are missing, for $1 \le n \le 10$ only. The RMSEs are in percent cloud albedo unit. The statistics are averages over all days and sites as in Fig. A1.

	n									
	1	2	3	4	5	6	7	8	9	10
R	0.999	0.998	0.997	0.996	0.994	0.993	0.991	0.990	0.988	0.986
RMSE	0.66	0.94	1.17	1.38	1.56	1.74	1.91	2.08	2.24	2.41
$f\|\text{Bias}\|$	0.03	0.05	0.06	0.07	0.08	0.09	0.10	0.11	0.12	0.13

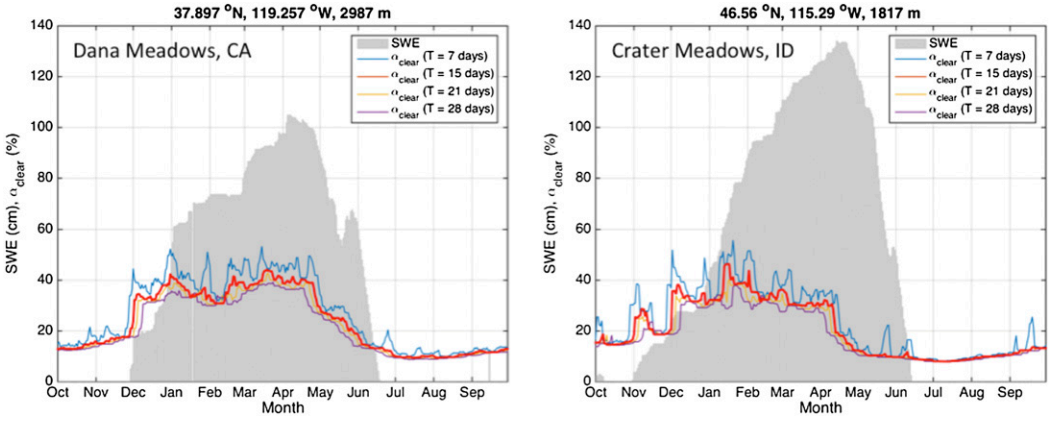

FIG. B1. Daily time series of water year 2006 SWE (gray shading) and of clear-sky albedo derived using four different time windows (color plots) at (left) Dana Meadows in Yosemite National Park, California, and (right) Crater Meadows in Idaho. The thick red line denotes the time window used in the study.

major changes while being immune to short-period changes.

There were a few isolated cases when the 15-day time window did not capture the evolving snow surface cover during the early snow season. For example, the period when snowfall and accumulation occurred rapidly between 29 November and 1 December 2005 was misclassified as no snow accumulation (Fig. 1).

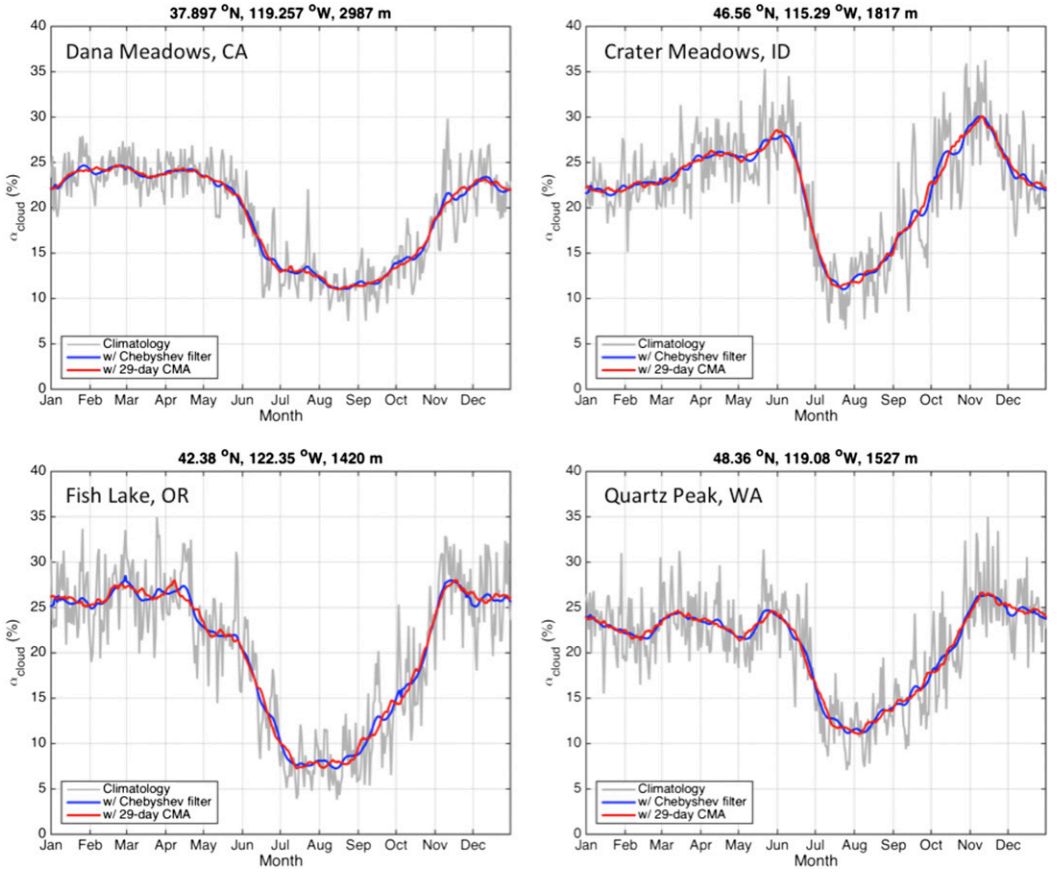

FIG. C1. Daily climatology (1996–2014) of α_{cloud} (gray) and its low-pass-filtered versions using Chebyshev Type I filter (blue) and original 29-day (±14 days) centered moving average (red) at four different locations.

Shortening the time window (e.g., to 7-day period) resolved this problem, but resulted in other days misclassified as cloud-free, for example, 2, 7, and 15 December 2005. On the other hand, expanding the time window would result in more days misclassified as no snow accumulation, for example, on 1–4 and 31 December 2005. Thus, we determined that 15-day window was optimal.

APPENDIX C

Determining the Seasonal Cycle

Harmonic fitting, Butterworth filter, and Chebyshev Type I filter were evaluated alongside the original 29-day (±14 days) centered moving average used in this study. Figure C1 shows the deseasonalized daily cloud albedo time series at four different pixels and two selected filters (first-order Chebyshev Type I filter, 29-day centered moving average), averaged over all years. The more sophisticated and computationally more intensive method yielded a somewhat different representation of the annual cycle, but without appreciable improvement. The power spectra of the deseasonalized time series displayed similar power dissipations at different spectral periods, most notably at ~365-day period (not shown).

The same conclusion was derived when different filters (i.e., harmonic fitting and Butterworth filter) and different orders (i.e., second, third, . . . , -order Chebyshev and 1, 2, 3, . . . , -point Butterworth) were used. Furthermore, the two other filters and the higher-order Chebyshev filters tended to underestimate the annual cycle as they produce dampened amplitudes, which resulted in large positive biases in winter and large negative biases in summer.

REFERENCES

Aguado, E., 1985: Radiation balances of melting snow covers at an open site in the central Sierra Nevada, California. *Water Resour. Res.*, **21**, 1649–1654, doi:10.1029/WR021i011p01649.

Bales, R. C., N. P. Molotch, T. H. Painter, M. D. Dettinger, R. Rice, and J. Dozier, 2006: Mountain hydrology of the western United States. *Water Resour. Res.*, **42**, W08432, doi:10.1029/2005WR004387.

Cano, D., J. M. Monget, M. Albuisson, H. Guillard, N. Regas, and L. Wald, 1986: A method for the determination of the global solar radiation from meteorological satellite data. *Sol. Energy*, **37**, 31–39, doi:10.1016/0038-092X(86)90104-0.

Cayan, D. R., K. T. Redmond, and L. G. Riddle, 1999: ENSO and hydrologic extremes in the western United States. *J. Climate*, **12**, 2881–2893, doi:10.1175/1520-0442(1999)012<2881:EAHEIT>2.0.CO;2.

Clemesha, R. E. S., A. Gershunov, S. F. Iacobellis, A. P. Williams, and D. R. Cayan, 2016: The northward march of summer low cloudiness along the California coast. *Geophys. Res. Lett.*, **43**, 1287–1295, doi:10.1002/2015GL067081.

Cline, D. W., 1997: Snow surface energy exchanges and snowmelt at a continental, midlatitude Alpine site. *Water Resour. Res.*, **33**, 689–701, doi:10.1029/97WR00026.

Dai, A., T. R. Karl, B. Sun, and K. E. Trenberth, 2006: Recent trends in cloudiness over the United States: A tale of monitoring inadequacies. *Bull. Amer. Meteor. Soc.*, **87**, 597–606, doi:10.1175/BAMS-87-5-597.

Davenport, E. C., and N. A. El-Sanhurry, 1991: Phi/Phimax: Review and synthesis. *Educ. Psychol. Meas.*, **51**, 821–828, doi:10.1177/0013164491051004003.

Davis, R. E., 1976: Predictability of sea surface temperature and sea level pressure anomalies over the North Pacific Ocean. *J. Phys. Oceanogr.*, **6**, 249–266, doi:10.1175/1520-0485(1976)006<0249:POSSTA>2.0.CO;2.

Dettinger, M. D., 2011: Climate change, atmospheric rivers, and floods in California—A multimodel analysis of storm frequency and magnitude changes. *J. Amer. Water Resour. Assoc.*, **47**, 514–523, doi:10.1111/j.1752-1688.2011.00546.x.

——, D. R. Cayan, H. F. Diaz, and D. M. Meko, 1998: North–south precipitation patterns in western North America on interannual-to-decadal time scales. *J. Climate*, **11**, 3095–3111, doi:10.1175/1520-0442(1998)011<3095:NSPPIW>2.0.CO;2.

Done, J., C. A. Davis, and M. Weisman, 2004: The next generation of NWP: Explicit forecasts of convection using the Weather Research and Forecasting (WRF) model. *Atmos. Sci. Lett.*, **5**, 110–117, doi:10.1002/asl.72.

Eastman, R., and S. G. Warren, 2013: A 39-yr survey of cloud changes from land stations worldwide 1971–2009: Long-term trends, relation to aerosols, and expansion of the tropical belt. *J. Climate*, **26**, 1286–1303, doi:10.1175/JCLI-D-12-00280.1.

Franzke, C., K. Fraedrich, and F. Lunkeit, 2001: Teleconnections and low-frequency variability in idealized experiments with two storm tracks. *Quart. J. Roy. Meteor. Soc.*, **127**, 1321–1339, doi:10.1002/qj.49712757411.

Gautier, C., G. Diak, and S. Masse, 1980: A simple physical model to estimate incident solar radiation at the surface from GOES satellite data. *J. Appl. Meteor.*, **19**, 1005–1012, doi:10.1175/1520-0450(1980)019<1005:ASPMTE>2.0.CO;2.

Gimeno García, S., T. Trautmann, and V. Venema, 2012: Reduction of radiation biases by incorporating the missing cloud variability via downscaling techniques: A study using the 3-D MoCaRT model. *Atmos. Meas. Tech.*, **5**, 2261–2276, doi:10.5194/amt-5-2261-2012.

Grubišić, V., and B. J. Billings, 2008: Climatology of the Sierra Nevada mountain-wave events. *Mon. Wea. Rev.*, **136**, 757–768, doi:10.1175/2007MWR1902.1.

Hannachi, A., 2004: *A Primer for EOF Analysis of Climate Data.* University of Reading, 33 pp.

Held, I. M., and B. J. Soden, 2006: Robust responses of the hydrological cycle to global warming. *J. Climate*, **19**, 5686–5699, doi:10.1175/JCLI3990.1.

Hinkelman, L. M., K. E. Lapo, N. C. Cristea, and J. D. Lundquist, 2015: Using CERES SYN surface irradiance data as forcing for snowmelt simulation in complex terrain. *J. Hydrometeor.*, **16**, 2133–2152, doi:10.1175/JHM-D-14-0179.1.

Holton, J., 2012: *An Introduction to Dynamic Meteorology.* 5th ed., Academic Press, 552 pp.

Howell, D. C., 2011: Chi-square test: Analysis of contingency tables. *International Encyclopedia of Statistical Science*, Springer, 250–252.

Iacobellis, S. F., and D. R. Cayan, 2013: The variability of California summertime marine stratus: Impacts on surface air temperatures. *J. Geophys. Res. Atmos.*, **118**, 9105–9122, doi:10.1002/jgrd.50652.

Ineichen, P., and R. Perez, 1999: Derivation of cloud index from geostationary satellites and application to the production of solar irradiance and daylight illuminance data. *Theor. Appl. Climatol.*, **64**, 119–130, doi:10.1007/s007040050116.

Kaiser, H. F., 1958: The varimax criterion for analytic rotation in factor analysis. *Psychometrika*, **23**, 187–200, doi:10.1007/BF02289233.

Kelly, D. L., J. T. Schaefer, and C. A. Doswell III, 1985: Climatology of nontornadic severe thunderstorm events in the United States. *Mon. Wea. Rev.*, **113**, 1997–2014, doi:10.1175/1520-0493(1985)113<1997:CONSTE>2.0.CO;2.

Khan, S. I., and Coauthors, 2011: Satellite remote sensing and hydrologic modeling for flood inundation mapping in Lake Victoria basin: Implications for hydrologic prediction in ungauged basins. *IEEE Trans. Geosci. Remote Sens.*, **49**, 85–95, doi:10.1109/TGRS.2010.2057513.

Kleissl, J., 2013: *Solar Energy Forecasting and Resource Assessment*. Academic Press, 462 pp.

Lapo, K. E., L. M. Hinkelman, M. S. Raleigh, and J. D. Lundquist, 2015: Impact of errors in the downwelling irradiances on simulations of snow water equivalent, snow surface temperature, and the snow energy balance. *Water Resour. Res.*, **51**, 1649–1670, doi:10.1002/2014WR016259.

Leathers, D. J., B. Yarnal, and M. A. Palecki, 1991: The Pacific/North American teleconnection pattern and United States climate. Part I: Regional temperature and precipitation associations. *J. Climate*, **4**, 517–528, doi:10.1175/1520-0442(1991)004<0517:TPATPA>2.0.CO;2.

Leavesley, G. H., R. W. Lichty, B. M. Troutman, and L. G. Saindon, 1983: Precipitation–runoff modeling system: User's manual. Water-Resources Investigations Rep. 83-4238, 206 pp. [Available online at http://pubs.usgs.gov/wri/1983/4238/report.pdf.]

Lorenz, E. N., 1956: Empirical orthogonal functions and statistical weather prediction. Statistical Forecasting Project Scientific Rep. 1, MIT Department of Meteorology, 49 pp.

Marks, D., and J. Dozier, 1992: Climate and energy exchange at the snow surface in the alpine region of the Sierra Nevada: 2. Snow cover energy balance. *Water Resour. Res.*, **28**, 3043–3054, doi:10.1029/92WR01483.

Markstrom, S. L., R. S. Regan, L. E. Hay, R. J. Viger, R. M. T. Webb, R. A. Payn, and J. H. LaFontaine, 2015: PRMS-IV, the precipitation–runoff modeling system, version 4. USGS Techniques and Methods Rep. 6–B7, 158 pp., doi:10.3133/tm6B7.

Mesinger, F., and Coauthors, 2006: North American Regional Reanalysis. *Bull. Amer. Meteor. Soc.*, **87**, 343–360, doi:10.1175/BAMS-87-3-343.

Mizukami, N., M. P. Clark, A. G. Slater, L. D. Brekke, M. M. Elsner, J. R. Arnold, and S. Gangopadhyay, 2014: Hydrologic implications of different large-scale meteorological model forcing datasets in mountainous regions. *J. Hydrometeor.*, **15**, 474–488, doi:10.1175/JHM-D-13-036.1.

Molotch, N. P., T. H. Painter, R. C. Bales, and J. Dozier, 2004: Incorporating remotely sensed snow albedo into spatially distributed snowmelt modeling. *Geophys. Res. Lett.*, **31**, L03501, doi:10.1029/2003GL019063.

Monahan, A. H., J. C. Fyfe, M. H. Ambaum, D. B. Stephenson, and G. R. North, 2009: Empirical orthogonal functions: The medium is the message. *J. Climate*, **22**, 6501–6514, doi:10.1175/2009JCLI3062.1.

Mote, P. W., 2006: Climate-driven variability and trends in mountain snowpack in western North America. *J. Climate*, **19**, 6209–6220, doi:10.1175/JCLI3971.1.

Norris, J. R., R. J. Allen, A. T. Evan, M. D. Zelinka, C. W. O'Dell, and S. A. Klein, 2016: Evidence for climate change in the satellite cloud record. *Nature*, **536**, 72–75, doi:10.1038/nature18273.

O'Gorman, P. A., and T. Schneider, 2008: The hydrological cycle over a wide range of climates simulated with an idealized GCM. *J. Climate*, **21**, 3815–3832, doi:10.1175/2007JCLI2065.1.

Paech, S. J., J. R. Mecikalski, D. M. Sumner, C. S. Pathak, Q. Wu, S. Islam, and T. Sangoyomi, 2009: A calibrated, high-resolution GOES satellite solar insolation product for a climatology of Florida evapotranspiration. *J. Amer. Water Resour. Assoc.*, **45**, 1328–1342, doi:10.1111/j.1752-1688.2009.00366.x.

Paulescu, M., E. Paulescu, P. Gravila, and V. Badescu, 2012: *Weather Modeling and Forecasting of PV Systems Operation*. Springer, 358 pp.

Pearson, K., 1895: Notes on regression and inheritance in the case of two parents. *Proc. Roy. Soc. London*, **58**, 240–242, doi:10.1098/rspl.1895.0041.

——, 1904: On the theory of contingency and its relation to association and normal correlation. *Drapers' Company Research Memoirs: Biometric Series I*, Dulau and Co., 46 pp.

Perez, R., P. Ineichen, K. Moore, M. Kmiecik, C. Chain, R. George, and F. Vignola, 2002: A new operational model for satellite-derived irradiances: Description and validation. *Sol. Energy*, **73**, 307–317, doi:10.1016/S0038-092X(02)00122-6.

——, S. Kivalov, A. Zelenka, J. Schlemmer, and K. Hemker Jr., 2010: Improving the performance of satellite-to-irradiance models using the satellite's infrared sensors. *Proc. of ASES Annual Conf.*, Phoenix, AZ, American Solar Energy Society, 8 pp. [Available online at http://www.asrc.cestm.albany.edu/perez/2010/ir.pdf.]

Pierce, D. W., and Coauthors, 2008: Attribution of declining western U.S. snowpack to human effects. *J. Climate*, **21**, 6425–6444, doi:10.1175/2008JCLI2405.1.

——, and D. R. Cayan, 2013: The uneven response of different snow measures to human-induced climate warming. *J. Climate*, **26**, 4148–4167, doi:10.1175/JCLI-D-12-00534.1.

Raleigh, M. S., K. Rittger, and J. D. Lundquist, 2011: What lies beneath? Comparing MODIS fractional snow covered area against ground-based observations under forest canopies and in the meadows of the Sierra Nevada. *Proc. 79th Western Snow Conf.*, Stateline, NV, Western Snow Conference, 3–14. [Available online at https://westernsnowconference.org/node/7.]

Ramanathan, V., R. D. Cess, E. F. Harrison, P. Minnis, B. R. Barkstrom, E. Ahmad, and D. L. Hartmann, 1989: Cloud-radiative forcing and climate: Results from the Earth Radiation Budget Experiment. *Science*, **243**, 57–63, doi:10.1126/science.243.4887.57.

Rauber, R. M., 1992: Microphysical structure and evolution of a central Sierra Nevada orographic cloud system. *J. Appl. Meteor.*, **31**, 3–24, doi:10.1175/1520-0450(1992)031<0003:MSAEOA>2.0.CO;2.

Richman, M. B., 1986: Rotation of principal components. *J. Climate*, **6**, 293–335, doi:10.1002/joc.3370060305.

Ringer, M. A., and K. P. Shine, 1997: Sensitivity of the Earth's radiation budget to interannual variations in cloud amount. *Climate Dyn.*, **13**, 213–222, doi:10.1007/s003820050161.

Rittger, K., A. Kahl, and J. Dozier, 2011: Topographic distribution of snow water equivalent in the Sierra Nevada. *Proc. 79th Western*

Snow Conf., Stateline, NV, Western Snow Conference, 37–46. [Available online at https://westernsnowconference.org/node/781.]

——, T. H. Painter, and J. Dozier, 2013: Assessment of methods for mapping snow cover from MODIS. *Adv. Water Resour.*, **51**, 367–380, doi:10.1016/j.advwatres.2012.03.002.

Rossow, W. B., C. Delo, and B. Cairns, 2002: Implications of the observed mesoscale variations of clouds for the Earth's radiation budget. *J. Climate*, **15**, 557–585, doi:10.1175/1520-0442(2002)015<0557:IOTOMV>2.0.CO;2.

Serreze, M. C., M. P. Clark, R. L. Armstrong, D. A. McGinnis, and R. S. Pulwarty, 1999: Characteristics of the western United States snowpack from snowpack telemetry (SNOTEL) data. *Water Resour. Res.*, **35**, 2145–2160, doi:10.1029/1999WR900090.

Seze, G., and W. B. Rossow, 1991: Time-cumulated visible and infrared radiance histograms used as descriptors of surface and cloud variations. *Int. J. Remote Sens.*, **12**, 877–920, doi:10.1080/01431169108929702.

Simpson, J. J., M. D. Dettinger, F. Gehrke, T. J. McIntire, and G. L. Hufford, 2004: Hydrologic scales, cloud variability, remote sensing, and models: Implications for forecasting snowmelt and streamflow. *Wea. Forecasting*, **19**, 251–276, doi:10.1175/1520-0434(2004)019<0251:HSCVRS>2.0.CO;2.

Smith, G. L., D. Rutan, and T. D. Bess, 1992: Atlas of albedo and absorbed solar radiation derived from *Nimbus 7* Earth Radiation Budget data set—November 1978 to October 1985. NASA Reference Publ. 1231, 64 pp. [Available online at https://ntrs.nasa.gov/archive/nasa/casi.ntrs.nasa.gov/19930001980.pdf.]

Smith, K., C. Strong, and S. Y. Wang, 2015: Connectivity between historical Great Basin precipitation and Pacific Ocean variability: A CMIP5 model evaluation. *J. Climate*, **28**, 6096–6112, doi:10.1175/JCLI-D-14-00488.1.

Thompson, D. W. J., and J. M. Wallace, 2000: Annular modes in the extratropical circulation. Part I: Month-to-month variability. *J. Climate*, **13**, 1000–1016, doi:10.1175/1520-0442(2000)013<1000:AMITEC>2.0.CO;2.

——, and ——, 2001: Regional climate impacts of the Northern Hemisphere annular mode. *Science*, **293**, 85–89, doi:10.1126/science.1058958.

U.S. Army Corps of Engineers, 1956: Snow hydrology: Summary report of the snow investigations. North Pacific Division, USACE, 437 pp.

Wallace, J. M., and D. S. Gutzler, 1981: Teleconnections in the geopotential height during the Northern Hemisphere winter. *Mon. Wea. Rev.*, **109**, 784–812, doi:10.1175/1520-0493(1981)109<0784:TITGHF>2.0.CO;2.

Warren, S. G., R. M. Eastman, and C. J. Hahn, 2007: A survey of changes in cloud cover and cloud types over land from surface observations, 1971–96. *J. Climate*, **20**, 717–738, doi:10.1175/JCLI4031.1.

Welch, R. M., K. S. Kuo, B. A. Wielicki, S. K. Sengupta, and L. Parker, 1988: Marine stratocumulus cloud fields off the coast of Southern California observed using Landsat imagery. Part I: Structural characteristics. *J. Appl. Meteor.*, **27**, 363–378, doi:10.1175/1520-0450(1988)027<0363:MSCFOT>2.0.CO;2.

Whiteman, C. D., 2000: *Mountain Meteorology: Fundamentals and Applications.* Oxford University Press, 376 pp.

Wilks, D. S., 1995: *Statistical Methods in Atmospheric Sciences: An Introduction.* Academic Press, 467 pp.

Yin, J. H., 2005: A consistent poleward shift of the storm tracks in simulations of 21st century climate. *Geophys. Res. Lett.*, **32**, L18701, doi:10.1029/2005GL023684.

Zelenka, A., R. Perez, R. Seals, and D. Renne, 1999: Effective accuracy of satellite-derived hourly irradiances. *Theor. Appl. Climatol.*, **62**, 199–207, doi:10.1007/s007040050084.